Applied Catalysis A, General 677 (2024) 119703

Contents lists available at ScienceDirect

Applied Catalysis A, General

journal homepage: www.elsevier.com/locate/apcata

Thermocatalytic decomposition of methane to low-carbon hydrogen using $LaNi_{1-x}Cu_xO_3$ perovskite catalysts

Zama G. Duma [a,*], Ashton Swartbooi [a], Nicholas M. Musyoka [b,*]

[a] HySA Infrastructure Centre of Competence, Centre for Nanostructures and Advanced Materials (CeNAM), Council for Scientific and Industrial Research (CSIR), Pretoria 0001, South Africa

[b] Nottingham Ningbo China Beacons of Excellence Research and Innovation Institute, University of Nottingham Ningbo China, Ningbo, Zhejiang 315100, China

ARTICLE INFO

Keywords:
Methane TCD
Low-carbon hydrogen
Perovskite
Gas Hourly Space Velocity
LaNiCuO3

ABSTRACT

The thermocatalytic decomposition (TCD) of methane is an attractive alternative to produce low-carbon hydrogen and solid carbonaceous materials. In this study, substituted $LaNi_{1-x}Cu_xO_3$ perovskite catalysts prepared via self-combustion method were investigated for methane TCD. The effect of Ni partial substitution with Cu, varying gas hourly space velocity, temperature and stability on methane conversions were evaluated. PXRD, H_2-TPR, SEM-EDS, TGA, and XPS were used to characterize the catalysts. An increase in Cu loading to 50%, increase in temperature and decrease in GHSV resulted in an improvement in methane conversions to 92%. At a GHSV of 2400 ml/g_{cat}.h, no significant deactivation was observed as the stability of the $LaNi_{0.5}Cu_{0.5}O_3$ catalyst increased from 6 to 20 hours' TOS with methane conversions maintained at 92% where carbon nanofibers were observed on the surface of the spent catalysts. The study demonstrates the potential to prepare $LaNi_{1-x}Cu_xO_3$ catalysts and identify optimal testing conditions for the novel production of low-carbon hydrogen with minimal catalyst deactivation.

1. Introduction

The production of hydrogen from natural gas, which consists mostly of methane (CH_4), is often associated with the simultaneous formation of carbon monoxide (CO) and carbon dioxide (CO_2). Whilst the former may be readily used in conversion processes to produce methanol, dimethyl ether, olefins, synthetic fuels, and other value-added compounds, CO_2 is a potent greenhouse gas that has been reported to contribute to climate change due to global warming. The current state-of-the-art route to produce hydrogen is the multistep steam methane reforming (SMR) process [1–3]. Conventionally, the process involves the use of steam to convert methane to synthesis gas, a mixture of hydrogen and carbon monoxide, at temperatures of 800–900 °C [4]. Thereafter, low-temperature and high-temperature water-gas shift catalytic reactions are carried out to convert carbon monoxide to carbon dioxide and hydrogen. The products are then separated using pressure-swing adsorption (PSA) and/or cryogenic distillation, among other methods [5]. Other processes employed to produce hydrogen include: autothermal reforming (ATR), where steam and oxygen are reacted with methane to form syngas; and partial oxidation (PO_x), where syngas is produced from methane and hydrogen [5]. However, all the processes listed have the drawback of producing hydrogen that is not COx-free. Furthermore, such mature processes are associated with high economic and operational costs. As such, the hydrogen produced cannot be used directly in Proton Exchange Membrane hydrogen fuel cells (PEM) because the CO_x contaminants poison the Pt electrode [6,7]. Also, due to side reactions, the nickel-based catalysts conventionally used in these processes suffer from deactivation due to coke formation which covers the active catalytic sites.

On the contrary, the thermocatalytic decomposition (TCD) of methane is a viable alternative and sustainable route to produce low-carbon or turquoise hydrogen. The latter refers to hydrogen produced directly from methane TCD [8]. Due to the anaerobic nature of the processes, TCD of methane has been reported to produce CO_x-free H_2 [9]. In addition, the process is associated with the simultaneous production of solid carbons such as nanocarbons as well as graphitic and amorphous carbons [8]. Albeit, carbon deposition often deactivates the catalyst, in TCD of methane, it can be fine-tuned to produce high-value carbons, thereby increasing the economic viability of the process [10].

While many catalysts have been investigated for the use in the TCD process, the optimal catalyst should ideally be able to operate for suitably long periods on stream under the formation of solids carbons

* Corresponding authors.
E-mail addresses: zduma@csir.co.za (Z.G. Duma), nicholas.musyoka@nottingham.edu.cn (N.M. Musyoka).

https://doi.org/10.1016/j.apcata.2024.119703
Received 10 January 2024; Received in revised form 7 March 2024; Accepted 20 March 2024
Available online 21 March 2024

[11–15]. In literature, it has been discussed that mixed-metal catalysts have synergistic advantages where one metal acts as the hydrogen production site, while the other eases carbon diffusion to minimize deactivation [16]. An alternative method is to develop catalysts that have oxygen vacancies on the surface, which allow for the carbon species to be oxidized as they are formed on the catalyst surface, through the movement of oxygen in the crystal lattice. Perovskite catalysts, usually of the form ABO_3, allow partial substitutions of the A and B sites, which can result in the formation of oxygen vacancies. This class of catalysts has a tunable, diverse structure as the A, B or O sites in the structure may be occupied by over 90% of the elements in the periodic table [17]. Perovskite catalysts have also been extensively investigated for the dry reforming of methane reactions but very few in literature have investigated perovskites for the methane TCD process [5,18–21]. Therefore, the focus of this article is the development of substituted perovskite catalysts of the form $LaNi_{1-x}Cu_xO_3$ with improved catalytic performance for the formation of CO_x-free, low-carbon or "turquoise" hydrogen.

2. Methods and materials

2.1. Catalyst synthesis

The perovskite catalyst in the form $LaNi_{1-x}Cu_xO_3$, where x denotes the percentage loading of Cu, was prepared by the self-combustion method as described by Gallego et al. [22]. In short, glycine (>98.5% purity, NH_2CH_2COOH, Associated Chemical Enterprises, Johannesburg, South Africa), used as ignition promoter, was added to an aqueous solution of the metal nitrates with the appropriate stoichiometry. The following nitrate salts were used: Cupric nitrate trihydrate (99.9% purity, $Cu(NO_3)_2.3\ H_2O$, Associated Chemical Enterprises, Johannesburg, South Africa), lanthanum nitrate hexahydrate (98% purity, $La(NO_3)_3.6\ H_2O$, Associated Chemical Enterprises, Johannesburg, South Africa), and nickel nitrate hexahydrate (98% purity, $Ni(NO_3)_2.6\ H_2O$, Laboratory BDH Reagents). Demineralized water was obtained from a water demineralization system (Thermo Fischer Barnstead Smart2Pure). The glycine amount was added to get a ratio of $NO_3/NH_2 = 1$. The resulting solution was slowly evaporated until a thick gel was obtained. Thereafter, the gel was heated, and subsequently ignited in a muffle furnace at 250 °C. The catalysts were then calcined at 700 °C for 8 h at a ramp rate of = 10 °C/min, which led to the formation of the perovskite structure. The catalysts were labelled according to the ratio of Ni to Cu i.e. $LaNi_{0.5}Cu_{0.5}O_3$ denotes 50 wt% loading of both Ni and Cu whereas $LaNi_{0.9}Cu_{0.1}O_3$ has 90 wt% loading of Ni and 10 wt% of Cu, respectively.

2.2. Characterization

Powder X-Ray Diffraction (PXRD) was used to determine the crystallinity of the catalysts using a Panalytical X'pert PRO PW 3040/60 diffractometer with a Cu Kα anode (λ = 0.1542 nm) operated at a generator voltage of 40 kV and tube current of 30 mA. The diffraction pattern was obtained at 3–90 ° at steps of 0.026 °/s. Scanning Electron Microscopy (SEM) was used for morphological analyses of the catalysts using an Auriga Cobra focused-ion beam Zeiss Ultra operated at an accelerating voltage of 2 kV. The samples were coated with carbon to prevent charging prior to analysis. For SEM-EDS, the accelerating voltage was increased to 15 kV. Hydrogen Temperature Programmed Reduction (H_2-TPR) was performed using a Micromeritics AutoChem II 2920 analyzer (Micromeritics Instrument Corporation, Norcross, GA, USA). Each catalyst, 50 mg, was placed between two-pieces of quartz wool in a U-shaped quartz tube. Thereafter, the catalysts were degassed at 150 °C at 10 °C/min with a hold time of 15 minutes under a constant flow of argon at 50 ml/min. After degassing, the temperature was decreased to 50 °C and then a 10% H_2/Ar mixture at 50 ml/min was introduced. The temperature was then increased to 900 °C at 10 °C/min and H_2 consumption monitored using a calibrated thermal conductivity detector (TCD). The thermal stability of the fresh and spent catalysts was analysed using a Mettler-Toledo TGA/SDTA 851^e analytical instrument where up to 10 mg of sample was loaded onto a platinum pan. Thereafter, the catalysts were heated at 10 °C/min from ambient temperature to 1000 °C in air at 90 ml/min and a nitrogen balance of 10 ml/min. X-Ray Photoelectron Spectroscopy (XPS) analysis was performed using a Thermo model ESCAlab 250 Xi instrument with a monochromatic Al Kα (1486.7 eV), 300 W X-ray power at $< 10^{-8}$ mBar pressure.

2.3. Catalysts testing

The catalysts were evaluated in a horizontal packed fixed-bed reactor, externally heated in a tube furnace. The reactor was made of stainless steel, with OD = 14 mm, ID = 12 mm and length 15 mm. Each catalyst was weighed out to 0.5 g and dispersed onto quartz wool, which acted as a stopper as well as gas dispersant. Argon was used as an inert gas to flush the system whilst the reactor attained the required temperature. The reactor was heated at 10 °C/min up to the required reaction temperature.

Prior to activity tests, the catalysts were reduced under a pure stream of hydrogen for 1.5 hours at 700 °C. After reduction, the system was flushed with Argon until the set reaction temperature was reached. After the operating temperature was reached, the gas was switched over to a stream of 95% methane at the required gas flow for the experiments. Argon was used a diluent at 5% as well as acting as an internal reference standard. The outgoing gas concentrations were measured with an online GC, model SCION 456 equipped with a flame ionization detector (FID) and thermal conductivity detector (TCD) using nitrogen as a carrier gas.

Methane conversion was calculated based on the results from the GC according to the following equation:

$$CH_4 \quad conversion \quad [\%] = \frac{[CH_4]_{in} - [CH_4]_{out}}{[CH_4]_{in}} * 100 \tag{1}$$

Where $[CH_4]_{in}$ and $[CH_4]_{out}$ denote the inlet and outlet molar concentrations of CH_4.

3. Results and discussion

3.1. Powder X-Ray diffraction

The XRD diffractograms of the calcined $LaNi_{1-x}Cu_xO_3$ catalysts are shown in Fig. 1. The catalysts show diffraction peaks at 2θ = 23.4°, 33°,

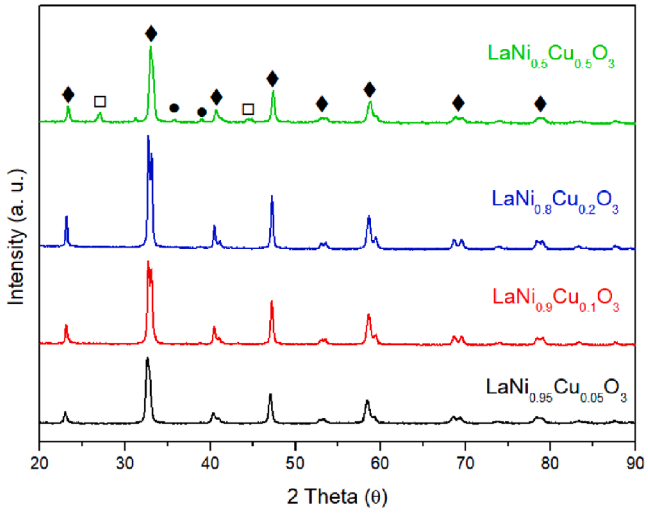

Fig. 1. XRD diffraction patterns of $LaNi_{0.95}Cu_{0.05}O_3$, $LaNi_{0.9}Cu_{0.1}O_3$, $LaNi_{0.8}Cu_{0.2}O_3$, and $LaNi_{0.5}Cu_{0.5}O_3$ catalysts. $LaNiO_3$ = ◆; La_2CuO_4 = □; CuO = ●.

40.7°, 47.6°, 53.3°, 58.9°, 68.9°, and 78.9° which are indicative of the $LaNiO_3$-like perovskite structure [23,24]. The diffraction pattern confirm the formation of rhombohedral $LaNiO_3$ structure [25]. The partial substitution of Ni with Cu in the perovskites becomes apparent when the Cu loading is increased to 50% (x = 0.5), in the $LaNi_{0.5}Cu_{0.5}O_3$ catalyst, where the additional peaks at 2θ = 27° and 44.6° indicate the presence of La_2CuO_4 crystalline phases [24]. Furthermore, the peaks at 2θ = 35.8° and 38.9° suggest the presence of CuO phases which indicate that the increase in Cu loading results in the formation of CuO nanoparticles in the perovskite structure [26]. As such, albeit all the calcined catalysts exhibit the $LaNiO_3$ perovskite-type phase, additional La_2CuO_4 and CuO phases are formed upon calcination when the Cu loading is increased to 50%, respectively.

3.2. Elemental composition

The theoretical and experimental composition of the catalysts, determined using SEM-EDS, are shown in Table 1. For all the $LaNi_{1-x}Cu_xO_3$ samples the theoretical and nominal composition were in close agreement. For instance, the $LaNi_{0.9}Cu_{0.1}O_3$ had a loading of 10 wt% Cu and 90 wt% Ni whereas the SEM-EDS analysis showed that there was a nominal loading of 9.5 wt% Cu and 90.5 wt% Ni, respectively. Similarly, the $LaNi_{0.5}Cu_{0.5}O_3$ catalyst had a theoretical loading of 50 wt% Cu and 50 wt% Ni whereas the nominal loading was found to be 49.8 wt% Cu and 50.2 Ni wt%. The SEM-EDS spectra of all the catalysts are shown in Figs. S1-S4.

3.3. Electron microscopy

The morphology of the catalysts is shown in the micrographs in Fig. 2 below. All the catalyst samples have similar consistent irregular shapes with interconnected channels. Furthermore, an increase in the Cu loading from 10% in $LaCu_{0.1}Ni_{0.9}O_3$ to 20% in $LaCu_{0.2}Ni_{0.8}O_3$ and 50% in $LaCu_{0.5}Ni_{0.5}O_3$ results in the formation of spherical nanoparticles that are dispersed over the bulk phase framework of the perovskite catalysts, Fig. 2e-h. The morphology of the perovskite catalysts shown is consistent with agglomerates that have been reported previously [23,27].

3.4. Hydrogen Temperature Programmed Reduction (H_2-TPR)

In the reduction of $LaNiO_3$ typical perovskites, Ni cations are reduced to metallic Ni whereas La_2O_3 is formed after H_2 reduction thereby essentially rendering Ni/La_2O_3 catalysts, as shown in Eq. 2-4 [5,28,29]. This is primarily because cations that occupy the A-sites in perovskite catalysts are less susceptible to reduction when compared to cations that occupy the B-sites. Furthermore, metallic Ni has been reported to be the active site for the decomposition of CH_4 [23]. The reduction of Ni in perovskite catalysts has been proposed to occur via the following reactions [30]:

$$2LaNiO_3 + H_2 \rightarrow La_2Ni_2O_5 + H_2O \quad (2)$$

$$La_2Ni_2O_5 + 2H_2 \rightarrow La_2O_3 + 2Ni + 2H_2O \quad (3)$$

$$2LaNiO_3 + 3H_2 \rightarrow 2Ni + La_2O_3 + 3H_2O \quad (4)$$

As such Ni^{3+} is reduced step wisely to Ni^0 i.e., Ni^{3+} to Ni^{2+} then to Ni^0 whereas La_2O_3 is formed as it occupies the A-site in the ABO_3 perovskite structure and is thus difficult to reduce at the set experimental conditions [29]. Therefore, due to the stable valence of the La A-site, two reduction peaks are anticipated due to the redox changes from Ni^{3+} to Ni^0 as corroborated by the TPR profiles in Fig. 3. The alpha (α) peaks between 336 °C and 390 °C in the $LaNiCuO_3$ catalysts are attributed to the reduction of Ni^{3+} to Ni^{2+} to form the $La_2Ni_2O_5$ phase shown in Eq. 2 whereas the beta (β) peaks between 522 °C and 537 °C correspond to the reduction of Ni^{2+} to the Ni^0 metallic phase which is active for CH_4 thermocatalytic decomposition [23,31]. The reduction of the catalysts results in Ni^0 particles dispersed on a La_2O_3 support as shown in Eq. 3.

In the $LaNiCuO_3$ perovskite catalysts, the reduction of Cu does not follow the same redox properties in pristine CuO due to its stabilization in the perovskites structure [21]. As such, the reduction of Cu^{2+} to Cu^0 overlaps with the reduction of Ni cations. Furthermore, the reduction of Cu^0 occurs at lower temperatures thereby facilitating hydrogen spillover which enhances the reduction of Ni^{3+} to Ni^{2+} [24]. As such, the alpha peaks have been reported to be an overlap of Ni^{3+} to Ni^{2+} and Cu^{2+} to Cu^{+1} whereas the beta peaks represent an overlap of Ni^{2+} to Ni^0 and Cu^{1+} to Cu^0, respectively [32]. In all the catalysts, except $LaCu_{0.5}Ni_{0.5}O_3$, an increase in the copper loading results in a shift to a lower reduction temperature of the α peaks from 390 °C to 336 °C probably due to the ease of reduction of Ni^{3+} species after the formation of Cu^0. A similar trend can be observed in the β peaks where the reduction temperature decreases gradually from 528 °C to 522 °C with an increase in copper loading.

In the case of $LaCu_{0.5}Ni_{0.5}O_3$, which has the highest copper loading, a similar trend in the ease of reduction shown by lower reduction temperatures of the α and β peaks can be observed in Fig. 3 and Table 2. However, due to the highest copper loading relative to the other catalysts, the hydrogen consumption was highest in the α peak which alludes to the reduction of Cu which then facilitates hydrogen spillover to the Ni cationic phases as shown by the consumption of 5.44 mmol/g in the α peak compared to 1.39 mmol/g in the β peak [33]. In the other perovskite catalysts, the hydrogen consumption in the α peaks (2.91–3.14 mmol/g) was lower than in the β peaks (4.03–4.66 mmol/g), respectively.

3.5. Catalytic performances

3.5.1. Effect of partial substitution of Ni with Cu

Previous studies such as the one conducted by Maneerung et al. varied the nickel content in perovskite catalyst with substitution by Co and Fe [21]. The study indicated, under pre-determined evaluation conditions, that the $LaNi_{0.8}Co_{0.2}O_3$ catalysts exhibited good performance. Albeit nickel and cobalt are very good active sites for thermocatalytic cracking reactions, the cost of Co is usually exorbitant. Conversely, Cu has also been shown to be a good catalyst when trying to minimize the formation of coke in the reforming process. As shown in the H_2-TPR data, Cu promoted Ni reduction and enhanced hydrogen spillover resulting in higher CH_4 conversions.

As shown in Fig. 4, there is a direct correlation between the Cu loading and CH_4 conversions i.e., an increase in the Cu loading in the perovskite catalyst results in an increase in CH_4 conversions. As such the catalysts with 5% and 10% Cu loading, $LaCu_{0.05}Ni_{0.95}O_3$ and $LaCu_{0.1}Ni_{0.9}O_3$, exhibited the lowest CH_4 conversions which stabilized at 5% whereas the $LaCu_{0.8}Ni_{0.2}O_3$ and $LaCu_{0.5}Ni_{0.5}O_3$ had the highest comparative conversions at 10–20%, respectively. Furthermore, the catalysts had high initial CH_4 conversions which dropped sharply within 25 minutes which indicates rapid deactivation of the perovskite catalysts which may be due to a high GHSV (8400 ml/g_{cat}.h), low residence time of CH_4 or coke deposition [31]. For catalytic evaluation, a relatively high GHSV was employed to observe the effect, in accordance with literature, on the stability of the perovskite catalysts. Furthermore, apart from produced hydrogen and unconverted CH_4, no by-products were detected in the effluent streams. As such, the single carbon atom

Table 1
Elemental loading of $LaNi_{1-x}Cu_xO_3$ catalysts.

Catalyst	Theoretical loading (Cu/Ni)	Experimental loading (Cu/Ni)
$LaNi_{0.95}Cu_{0.05}O_3$	0.05	0.052
$LaNi_{0.9}Cu_{0.1}O_3$	0.1	0.11
$LaNi_{0.8}Cu_{0.2}O_3$	0.2	0.19
$LaNi_{0.5}Cu_{0.5}O_3$	1	0.99

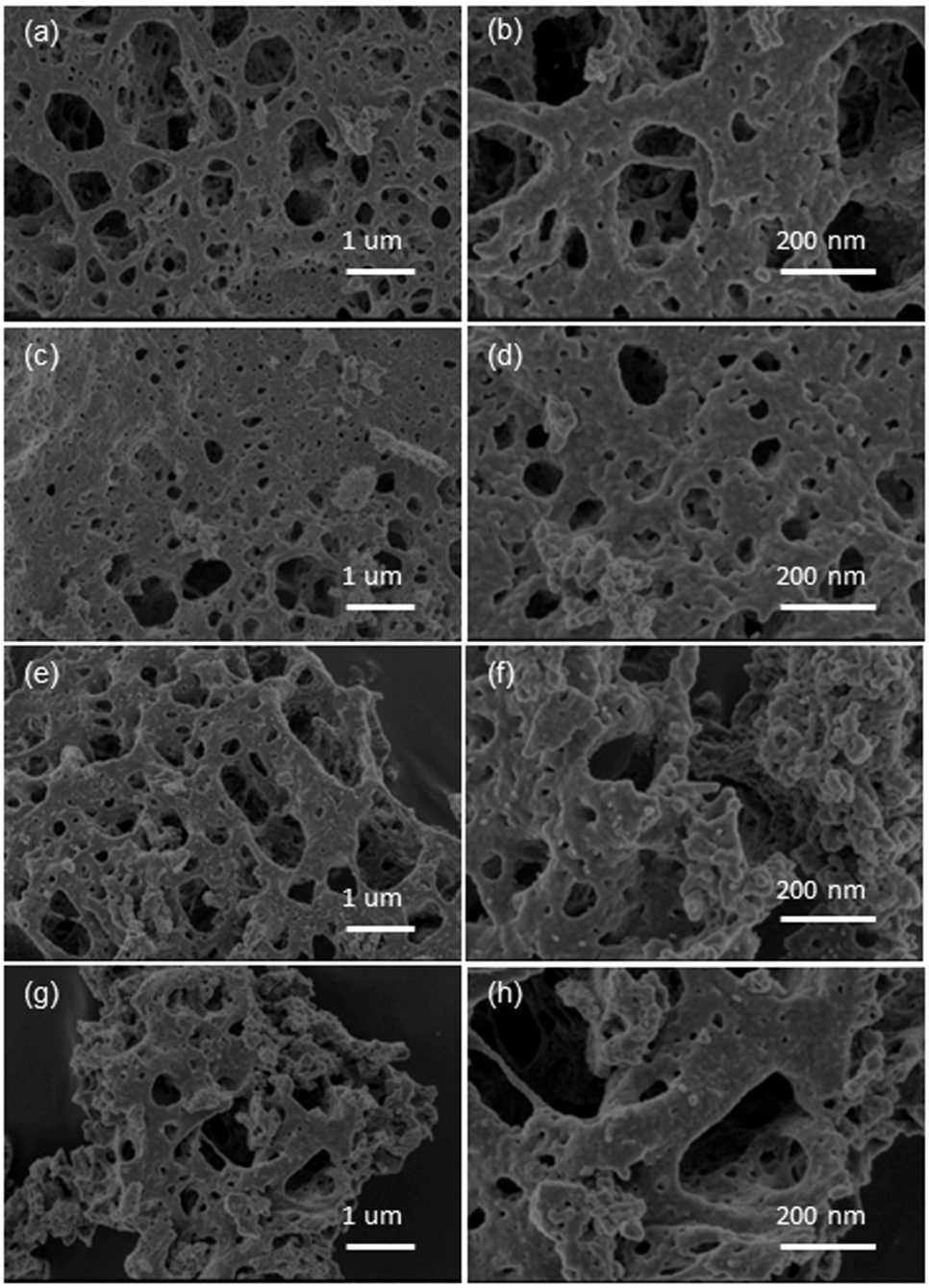

Fig. 2. SEM micrographs of: (a-b) $LaCu_{0.05}Ni_{0.95}O_3$; (c-d) $LaCu_{0.1}Ni_{0.9}O_3$; (e-f) $LaCu_{0.2}Ni_{0.8}O_3$; and (g-h) $LaCu_{0.5}Ni_{0.5}O_3$.

in the CH_4 molecule results in the formation of solid carbon as the only by-product [34]. In addition, the rapid deactivation of the catalysts may be due to the encapsulation of Ni^0 active sites by solid carbon formed during CH_4 decomposition which may be circumvented by use of fluidized-bed reactors where there is a continuous replacement of spent catalysts [35,36]. Furthermore, a study by Suelvels et al. found that deactivation by thermal sintering in fixed bed reactors was less than that caused by the formation of highly-ordered carbons [37].

3.5.2. *Effect of GHSV*

Due to the relatively better catalytic performance by the $LaCu_{0.5}Ni_{0.5}O_3$ catalyst observed in Fig. 4 at 8400 ml/g_{cat}.h and 900 °C, the effect of GHSV on CH_4 conversion was investigated using this catalyst. Three different GHSV's were evaluated whereas the effect on CH_4 conversion is shown in Fig. 5. As previously highlighted, the sharp decrease in initial CH_4 conversions may be attributed to the formation of coke on the catalyst surface [38]. At high GHSVs, the diffusion of CH_4 in the catalyst pores is superseded by the formation of carbon on the surface, resulting in the formation of solid carbon allotropes on the active sites [39].

At the lowest GHSV tested, close to 92% CH_4 conversion was achieved for the full operation of up to 20 hours on stream. The stability of the catalyst is evident, as very little deactivation, with respect to CH_4 conversion, occurred over the evaluation period. The stability of the catalyst is also attributed to the very stable La_2O_3 support, which assists with carbon formations and diffusion. The diffusion of carbon species onto the surface is a very important step when trying to produce valued-added carbons. Liu et al. have shown that a Ni-based catalyst contributes to very high hydrogen yields, but a different transition metal is required, such as Fe, to produce nanotubes [40]. This is due to the diffusion of

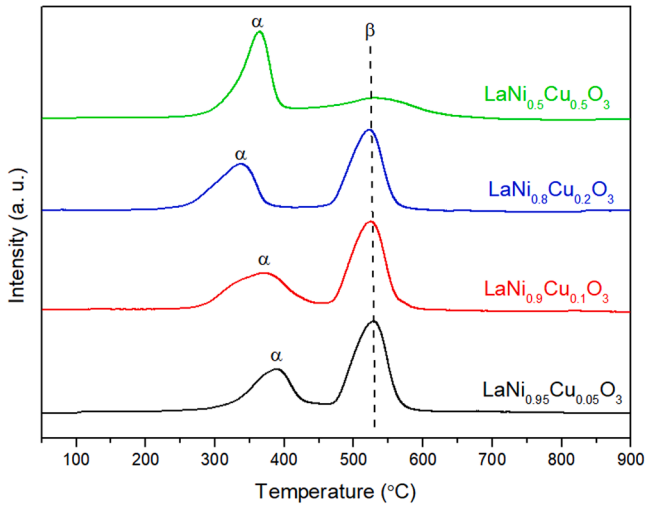

Fig. 3. H_2-TPR profiles of $LaNi_{0.95}Cu_{0.05}O_3$, $LaNi_{0.9}Cu_{0.1}O_3$, $LaNi_{0.8}Cu_{0.2}O_3$, and $LaNi_{0.5}Cu_{0.5}O_3$ catalysts.

Table 2
Reduction temperature and hydrogen consumption of the perovskite catalysts.

Perovskite catalyst	Peak	Reduction temperature (°C)	Hydrogen consumption (mmol/g)
$LaNi_{0.95}Cu_{0.05}O_3$	α	390	3.13
	β	528	4.66
$LaNi_{0.9}Cu_{0.1}O_3$	α	371	3.14
	β	524	4.39
La $Ni_{0.8}Cu_{0.2}O_3$	α	336	2.91
	β	522	4.03
$LaNi_{0.5}Cu_{0.5}O_3$	α	364	5.44
	β	537	1.39

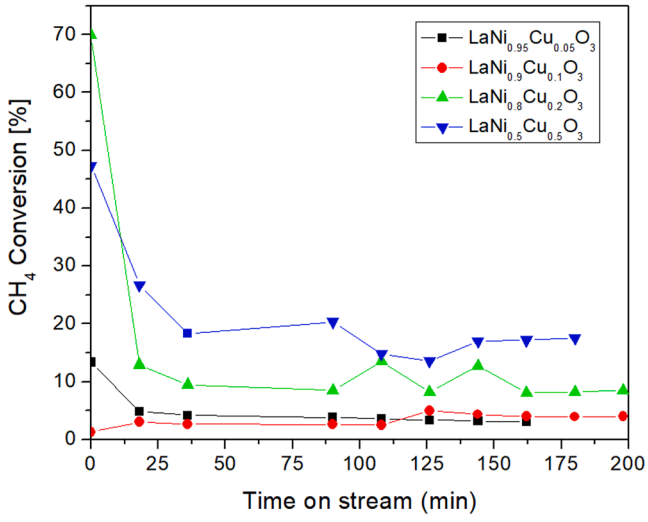

Fig. 4. CH_4 conversions of the perovskite catalysts at various Cu loading. GHSV = 8400 ml/g_{cat}.h, T = 900 °C.

carbon onto the Fe, which is faster than on Ni, respectively. However, SEM analysis of the spent $LaCu_{0.5}Ni_{0.5}O_3$ catalyst evaluated at 2400 ml/g_{cat}.h showed the formation of carbon fibres and filaments, Fig. 6. The simultaneous formation of solid carbons and sustained high CH_4 conversion may be due to a tip growth mechanism where the reduced Ni^0 active sites remain exposed and available for continuous CH_4 decomposition [31,41].

The thermal stability of the spent $LaNi_{0.5}Cu_{0.5}O_3$ perovskite catalyst

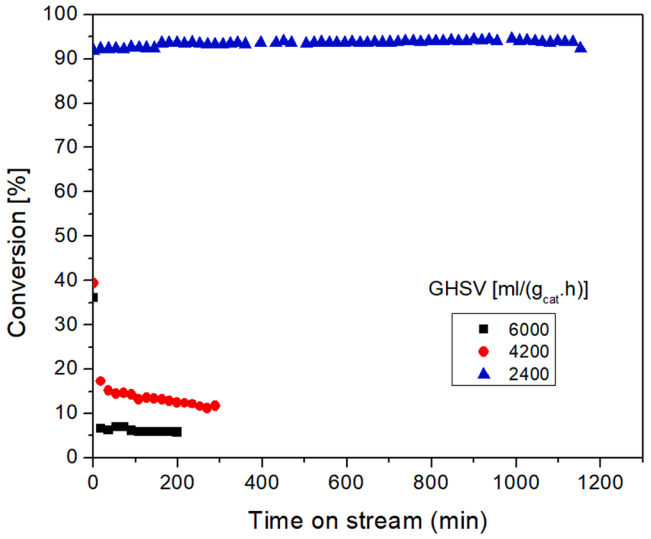

Fig. 5. CH_4 conversions of $LaNi_{0.5}Cu_{0.5}O_3$ catalyst at GHSVs = 2400, 4200, and 6000 ml/g_{cat}.h.

was also tested as shown by the thermogram in Fig. 7. The TGA and derivative TGA profile exhibit three distinct weight loss steps. The 1.8% weight loss peak at 316 °C is due to the combustion of amorphous or less crystalline graphitic carbon whereas the minimal weight loss (0.2%) below 200 °C is due to physisorbed water or moisture [22]. The sharp weight change of 64.7% observed at 586 °C and 695 °C is attributed to the combustion of crystalline or highly ordered graphitic carbon. The TGA results further corroborate the SEM micrographs wherein filamentous carbon can be observed. Post 700 °C, complete oxidation of the solid carbon has occurred resulting in the perovskite-type catalyst which is stable up 1000 °C [42,43]. The TGA profiles of the pristine fresh catalysts in air are shown in Figure S5 where no more than 6% weight loss was observed which indicates that the perovskite catalysts have high thermal stability.

The thermocatalytic decomposition of CH_4 to hydrogen and solid carbons observed in Fig. 6 has been proposed to occur via a multistep process which can be broken down to elementary steps where there is dissociative adsorption of CH_4 on the active sites of the catalyst. For instance, Chen et al. proposed the following mechanism:

Methane dissociation:

$$CH_4 + 2S \leftrightarrow CH_3 - S + H - S \quad (5)$$

$$CH_3 - S + S \leftrightarrow CH_2 - S + H - S \quad (6)$$

$$CH_2 - S + S \leftrightarrow CH - S + H - S \quad (7)$$

$$CH - S + S \leftrightarrow C - S + H - S \quad (8)$$

$$2H - S \leftrightarrow H_2 + 2S \quad (9)$$

Dissolution/Segregation:

$$C - S \leftrightarrow C_{Ni.f} + S \quad (10)$$

Diffusion of carbon through nickel:

$$C_{Ni.f} \leftrightarrow C_{Ni.r.} \quad (11)$$

Precipitation/dissolution of carbon:

$$C_{Ni.r} \leftrightarrow C_{f.} \quad (12)$$

Encapsulating carbon formation:

$$nC - S \leftrightarrow C_{encapsulating} \quad (13)$$

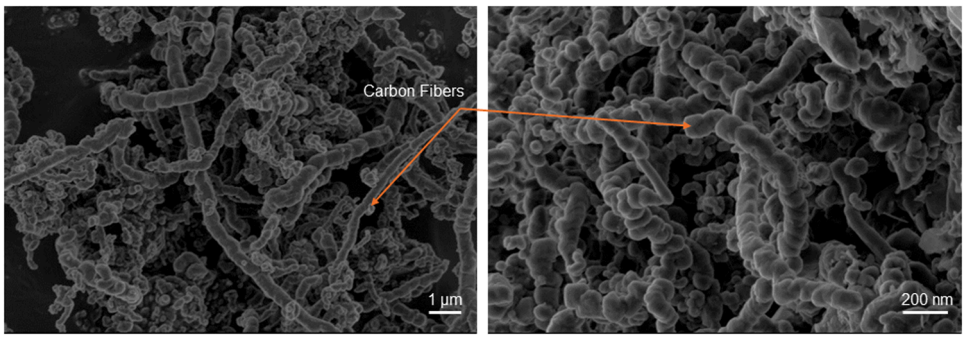

Fig. 6. SEM micrographs of spent $LaNi_{0.5}Cu_{0.5}O_3$ catalyst evaluated at GHSV = 2400 ml/g_{cat}.h, and T = 900 °C.

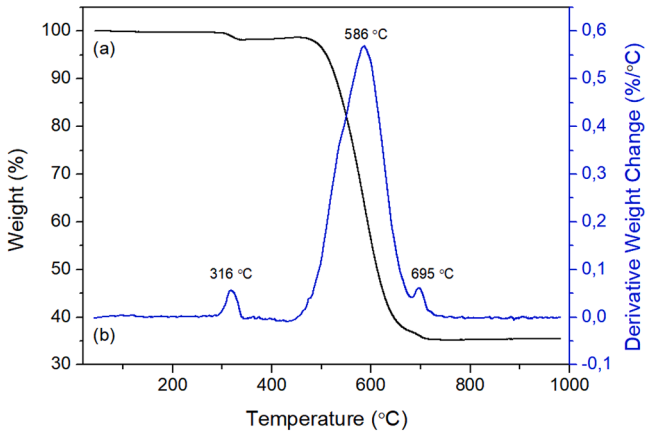

Fig. 7. (a) TGA, and (b) Derivate TGA profiles of spent $LaNi_{0.5}Cu_{0.5}O_3$ catalyst.

Where S refers to an adsorption site on the catalyst, $C_{Ni,f}$ denotes carbon dissolved in the front part of a nickel particle, $C_{Ni,r}$ refers to carbon dissolved in the portion of the nickel particle that is in contact with the support, and $C_{encapsulating}$ represents the carbon that encapsulates the Ni particles thereby deactivating the catalyst [44]. Due to the little deactivation of the $LaNi_{0.5}Cu_{0.5}O_3$ after 20 h online, Fig. 5., it may assumed that the carbonaceous deposits are of nanofiber morphology [38].

XPS analysis of the fresh and spent $LaNi_{0.5}Cu_{0.5}O_3$ catalyst was used to discern the surface composition of the constituents. Fig. 8a shows the XPS spectrum of La 3d where the peaks at 838.6, 837.7, 835.1, and 833.1 eV binding energy (BE) are attributed to the La $3d_{5/2}$ orbitals [29, 30,45]. The peaks are attributed to the La^{3+} state in A site of the perovskite. In the spent catalysts, a doublet peak can be observed at 836.7 and 840.2 eV which have been assigned to La $3d_{5/2}$ photoelectrons of the $La_2(C_2O_4)_3$ species. The shift in the photoelectrons may be due to the change in the coordination environment of La^{3+} as a result of the formed carbon filaments formed by the methane TCD reaction [29]. Due to the overlapping peaks of La $3d_{3/2}$ and Ni $2p_{3/2}$ peaks between 870 and 845 eV as well as the insertion if Ni^{2+} and Ni^{3+} into the perovskite structure, the photoelectron peaks of Ni species were not detected on the surface of the fresh and spent catalysts. It has, however, been reported in literature that the peaks between 855 and 853 eV belong to Ni^{2+} and Ni^{3+} species which in this instance overlaps with La $3d_{3/2}$ photoelectron peaks [45]. Furthermore, it can be seen from the spectrum in Fig. 8b that Cu 2p exhibits a photoelectron peak at 933.6 eV attributed to Cu $2p_{3/2}$. The satellite peak between 946 and 940 eV as well as the peak at 954 eV suggest that Cu^{2+} is the dominant species in the catalysts which is consistent with the H_2-TPR results observed in Fig. 3 [46]. Interestingly, no Cu photoelectron peaks were observed in the spent $LaNi_{0.5}Cu_{0.5}O_3$ catalyst which may allude to surface coverage by the carbon fibres observed in Fig. 6 [47]. Indeed, as shown in Table 3, 92% of the surface on the spent catalyst consists of atomic carbon compared to 37.3% in the fresh catalyst.

The O 1 s spectrum of the fresh $LaNi_{0.5}Cu_{0.5}O_3$ is shown in Fig. 8c. The spectrum was deconvoluted to four main peaks with distinct BEs: 533.3 eV which is due to the photoelectrons from O atoms in physisorbed moisture on the surface ($O_{moisture}$); 531.4 eV due to chemisorbed surface carbonate species in the basic A sites of the perovskite (O_{ads}); 529.1 and 528.3 eV which are assigned to metal oxides where oxygen atoms in the lattice of the structure are bonded to the cations (O_{latt}) [30, 45,48]. The O_{ads} species, chemisorbed surface oxygen, are generally attributed to oxygen vacancies which are more reactive than O_{latt} species [49]. Therefore, the surface concentration ratio of the more reactive O_{ads} was calculated as a proportion of the atomic concentration over the total oxygen concentration i.e. O_{ads}/O_{all}. The latter was found to be 61.1% in comparison to a cumulative 33% (O_{latt}) and 5.9% physisorbed oxygen, Table 3. In the XPS spectrum of the spent catalyst, 100% of the O1s peaks belonged to the O_{ads} species, at 532 eV, albeit the overall atomic concentration decreased to 6.4% from 46.7% in the fresh catalyst. Indeed, the O_{latt} species bonded to the cations were not detected on the surface which is consistent with the decrease in La^{3+} surface concentration from 21% to 1.4% whereas no Cu^{2+} was detected in the spent catalysts. The formation of the carbon nanofilaments observed in Figs. 6–7 are further corroborated by the C 1 s XPS spectrum in the spent catalyst where a well-defined peak at 284 eV indicative of sp^2 hybridized graphitic-type carbon was observed, Fig. 8d [47]. This observation is consistent with the high surface composition of carbon as shown in Table 3.

3.5.3. *Effect of temperature*

The decomposition of CH_4 to H_2 and solid nanocarbons is an endothermic reaction as can be seen from Eq. 5 [50]. As such, an increase in temperature is expected to result in an increase in CH_4 conversions. As shown in Fig. 9, a decrease in reaction temperature had the expected result of a decline in CH_4 conversion. The stability of the catalyst under these conditions is evident, with very little loss in activity. For the tests run at 700 °C, the conversion decreased from a peak of 74–69%, while in the test at 800 °C dropped from 89% to 82%. Interestingly, for the reaction at 900 °C, there was no decrease in the conversions, as it maintained the same conversion over the entire evaluation period. The effect of temperature on CH_4 decomposition has also been investigated by Suelvels et al. where an increase in reaction temperature from 550 °C to 700 °C resulted in an increase in CH_4 conversions from 10.2% to 31.2%. However, at higher temperatures, the rate of carbon deposition increases which deactivates the catalysts [37]. Furthermore, a similar effect of temperature on CH_4 conversion has been previously observed i.e. using an $LaNiO_3$ catalyst where Maneerung et al. reported that an increase in temperature increased CH_4 conversions [31]. The study reported CH_4 conversions of 42% at 600 °C, 60% at 650 °C, 65% at 700 °C, 80% at 750 °C, and 92 °C at 800 °C. In addition, Gallego et al. also reported CH_4 conversion of 60% at 600 °C which increased to 80% at 700 °C using a $LaNiO_3$ catalyst prepared using a self-combustion method, Table 4 [22]. Furthermore, Rivas et al. also noted an increase in CH_4

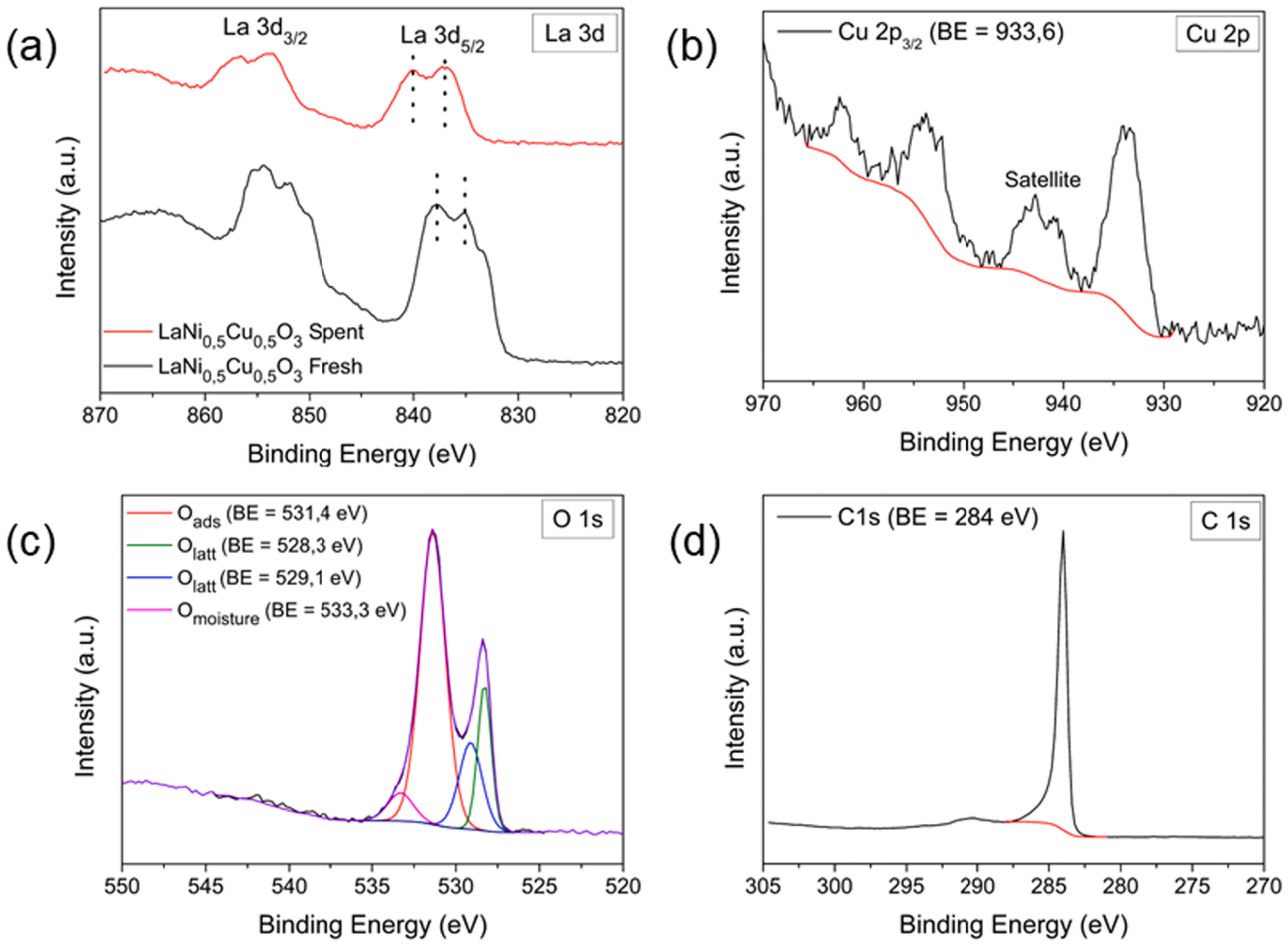

Fig. 8. XPS spectra of (a) La 3d in fresh and spent catalyst, (b) Cu 2p in fresh catalyst, (c) O 1 s in fresh catalyst, and (d) C 1 s in spent catalyst.

Table 3
XPS surface composition and oxygen ratio of fresh and spent $LaNi_{0.5}Cu_{0.5}O_3$ catalyst.

$LaNi_{0.5}Cu_{0.5}O_3$ catalyst	At (%)					Surface oxygen percentage (at%)[a]
	La	Ni	Cu	O	C	O_{ads}/O_{all}
Fresh	11.2	nd[b]	4.8	46.7	37.3	61.1
Spent	1.3	nd	nd	6.4	92	100

[a] $O_{all} = O_{moisture} + O_{ads} + O_{latt}$
[b] nd = not detected

conversion with temperature in $LaNi_{0.95}Rh_{0.05}O_3$ catalysts from 28% at 450 °C and 200 h^{-1} to 50% at 650 °C and 100 h^{-1}. A similar effect of temperature was observed for a co-precipitated $LaNiO_3$ catalyst where CH_4 conversion of 15% at 450 °C increased to 30% at 650 °C [38].

$$CH_4 \leftrightarrow 2H_2 + C_s \Delta H = +74.9 kJ/mol \quad (14)$$

The thermodynamic limit for the decomposition of CH_4 to H_2 was modelled using HSC Chemistry software, 1 mol of CH_4 was used as a feed, and stepwise increments for temperature up to 1000 °C, Fig. 10. The data was compared with average conversion at each temperature from the experimental results, Fig. 9. The experimental conversions of catalysts tested was very close to the thermodynamic limit for the set temperature, at a given GHSV.

4. Conclusion

In this work, the thermocatalytic decomposition of CH_4 to produce

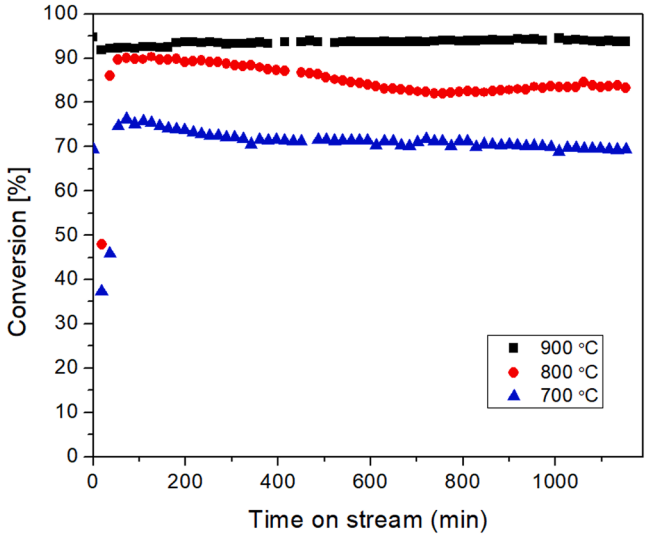

Fig. 9. CH_4 conversions of $LaNi_{0.5}Cu_{0.5}O_3$ catalysts at various temperatures. GHSV = 2400 ml/g_{cat}.h.

CO_x-free H_2 was studied by investigating the effect of partial substitution of Cu into a $LaNiO_3$ perovskite catalyst which was tested under various Cu loadings, GHSV's and temperatures. It was found that increasing Cu loading to 50% in $LaNi_{0.5}Cu_{0.5}O_3$ catalysts and decreasing GHSV enhances CH_4 conversion and stability with minimal deactivation. An

Table 4
Comparison of CH_4 conversions of $LaNiO_3$-type catalysts with the $LaNi_{0.5}Cu_{0.5}O_3$ catalyst reported in this work.

Catalyst	Temperature (°C)	GHSV	Maximum CH_4 conversion (%)	Reference
$LaNi_{0.5}Cu_{0.5}O_3$	700	2	74	This work
	800	400 ml/	89	
	900	g.h	92	
$LaNiO_3$	600	8.2 L/g.h	65	[22]
	700	7.5 L/g.h	80	
$LaNiO_3$	600	12 000 h^{-1}	42	[31]
	650		60	
	700		65	
	750		80	
	800		92	
$LaNiO_3$-sg[a]	450	200 h^{-1}	15	[38]
	650	100 h^{-1}	30	
$LaNi_{0.95}Rh_{0.05}O_3$-cp[b]	450	200 h^{-1}	28	
	650	100 h^{-1}	50	

[a] sg = Sol-gel preparation method
[b] cp = Co-precipitation preparation method

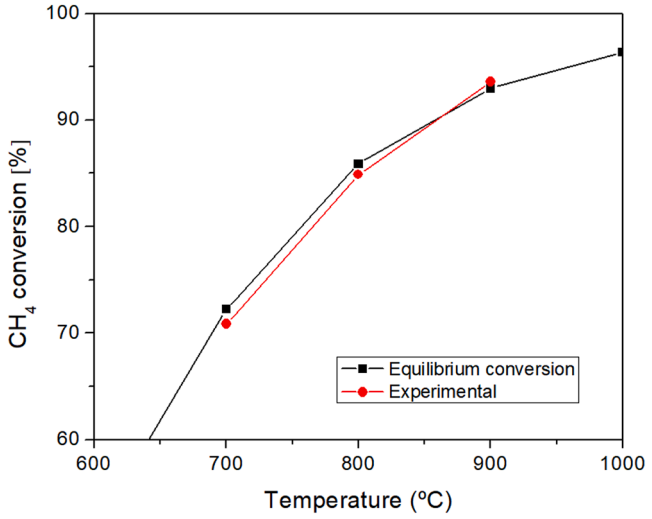

Fig. 10. Experimental and equilibrium conversions of CH_4 at various temperatures.

increase in the testing temperature also increases CH_4 conversions. Noteworthy, when compared to Cu loading and temperature, GHSV was found to have the most pronounced improvement in CH_4 conversions. The conversion enhancement reached 92% which was sustained for over more than 20 hours of the catalyst on stream, even under a pure flow of CH_4. Furthermore, XPS revealed high oxygen vacancies in the catalyst which may explain the comparatively large increase in CH_4 conversions and stability which resulted in carbon nanofibers observed using SEM, XPS, and TGA. The results indicate that from a pure stream of CH_4, sustainable, CO_x-free, low-carbon or "turquoise" hydrogen can be produced without significant deactivation of the perovskite catalyst.

CRediT authorship contribution statement

Zama Duma: Writing – review & editing, Writing – original draft, Investigation, Formal analysis, Data curation. **Ashton Swartbooi:** Writing – review & editing, Investigation, Formal analysis, Data curation, Conceptualization. **Nicholas Musyoka:** Supervision, Project administration, Funding acquisition.

Declaration of Competing Interest

The authors declare that they have no known competing financial interests or personal relationships that could have appeared to influence the work reported in this paper

Data Availability

Data will be made available on request.

Acknowledgements

The authors would like to thank the Council for Scientific and Industrial Research, and the Department of Science and Innovation's Hydrogen South Africa (DSI-HySA) Infrastructure for the funding of the biogas-to-hydrogen project (Grant number: C6G0097). The authors would like to extend gratitude to the Energy and Fuels for a Sustainable Environment Team, Institut de Chimie et Procédés pour l'Energie, l'Environnement et la Santé, Université de Strasbourg for the access to advanced H_2-TPR analyses.

Appendix A. Supporting information

Supplementary data associated with this article can be found in the online version at doi:10.1016/j.apcata.2024.119703.

References

[1] S. Poto, F. Gallucci, M. Fernanda Neira d'Angelo, Direct conversion of CO2 to dimethyl ether in a fixed bed membrane reactor: Influence of membrane properties and process conditions, Fuel 302 (2021) 121080.
[2] F. Pontzen, W. Liebner, V. Gronemann, M. Rothaemel, B. Ahlers, CO2-based methanol and DME – Efficient technologies for industrial scale production, Catal. Today 171 (2011) 242–250.
[3] M. De Falco, M. Capocelli, G. Centi, Dimethyl ether production from CO2 rich feedstocks in a one-step process: Thermodynamic evaluation and reactor simulation, Chem. Eng. J. 294 (2016) 400–409.
[4] T.I. Korányi, M. Németh, A. Beck, A. Horváth, Recent advances in methane pyrolysis: turquoise hydrogen with solid carbon production, Energies 15 (2022) 6342.
[5] Z. Bian, Z. Wang, B. Jiang, P. Hongmanorom, W. Zhong, S. Kawi, A review on perovskite catalysts for reforming of methane to hydrogen production, Renew. Sustain. Energy Rev. 134 (2020) 110291.
[6] S.K. Saraswat, K.K. Pant, Ni–Cu–Zn/MCM-22 catalysts for simultaneous production of hydrogen and multiwall carbon nanotubes via thermo-catalytic decomposition of methane, Int. J. Hydrog. Energy 36 (2011) 13352–13360.
[7] A. Venugopal, S. Naveen Kumar, J. Ashok, D. Hari Prasad, V. Durga Kumari, K.B. S. Prasad, M. Subrahmanyam, Hydrogen production by catalytic decomposition of methane over Ni/SiO2, Int. J. Hydrog. Energy 32 (2007) 1782–1788.
[8] J.C. Guevara, J.A. Wang, L.F. Chen, M.A. Valenzuela, P. Salas, A. García-Ruiz, J. A. Toledo, M.A. Cortes-Jácome, C. Angeles-Chavez, O. Novaro, Ni/Ce-MCM-41 mesostructured catalysts for simultaneous production of hydrogen and nanocarbon via methane decomposition, Int. J. Hydrog. Energy 35 (2010) 3509–3521.
[9] J. Ashok, G. Raju, P.S. Reddy, M. Subrahmanyam, A. Venugopal, Catalytic decomposition of CH4 over NiO–Al2O3–SiO2 catalysts: Influence of catalyst preparation conditions on the production of H2, Int. J. Hydrog. Energy 33 (2008) 4809–4818.
[10] H.Y. Wang, E. Ruckenstein, Formation of filamentous carbon during methane decomposition over Co–MgO catalysts, Carbon 40 (2002) 1911–1917.
[11] R. Aiello, J.E. Fiscus, H.-C. zur Loye, M.D. Amiridis, Hydrogen production via the direct cracking of methane over Ni/SiO2: catalyst deactivation and regeneration, Appl. Catal. A: Gen. 192 (2000) 227–234.
[12] M. Msheik, S. Rodat, S. Abanades, Methane cracking for hydrogen production: a review of catalytic and molten media pyrolysis, Energies 14 (2021) 3107.
[13] A. Amin, W. Epling, E. Croiset, Reaction and deactivation rates of methane catalytic cracking over nickel, Ind. Eng. Chem. Res. 50 (2011) 12460–12470.
[14] A.M. Amin, E. Croiset, W. Epling, Review of methane catalytic cracking for hydrogen production, Int. J. Hydrog. Energy 36 (2011) 2904–2935.
[15] L. Weger, A. Abánades, T. Butler, Methane cracking as a bridge technology to the hydrogen economy, Int. J. Hydrog. Energy 42 (2017) 720–731.
[16] M. McConnachie, M. Konarova, S. Smart, Literature review of the catalytic pyrolysis of methane for hydrogen and carbon production, Int. J. Hydrog. Energy (2023).
[17] H. Arandiyan, P. Sudarsanam, S.K. Bhargava, A.F. Lee, K. Wilson, Perovskite catalysts for biomass valorization, ACS Catal. (2023) 7879–7916.

[18] J.A. Gómez-Cuaspud, E. Vera-López, J.B. Carda-Castelló, E. Barrachina-Albert, One-step hydrothermal synthesis of LaFeO 3 perovskite for methane steam reforming, React. Kinet., Mech. Catal. 120 (2017) 167–179.
[19] S. Moogi, C. Hyun Ko, G. Hoon Rhee, B.-H. Jeon, M. Ali Khan, Y.-K. Park, Influence of catalyst synthesis methods on anti-coking strength of perovskites derived catalysts in biogas dry reforming for syngas production, Chem. Eng. J. 437 (2022) 135348.
[20] G.R. Moradi, F. Khosravian, M. Rahmanzadeh, Effects of partial substitution of Ni by Cu in LaNiO3 perovskite catalyst for dry methane reforming, Chin. J. Catal. 33 (2012) 797–801.
[21] T. Maneerung, K. Hidajat, S. Kawi, Co-production of hydrogen and carbon nanofibers from catalytic decomposition of methane over LaNi(1−x)Mx O3−α perovskite (where M = Co, Fe and X = 0, 0.2, 0.5, 0.8, 1), Int. J. Hydrog. Energy 40 (2015) 13399–13411.
[22] G.Sierra Gallego, J. Barrault, C. Batiot-Dupeyrat, F. Mondragón, Production of hydrogen and MWCNTs by methane decomposition over catalysts originated from LaNiO3 perovskite, Catal. Today 149 (2010) 365–371.
[23] F. Touahra, A. Rabahi, R. Chebout, A. Boudjemaa, D. Lerari, M. Sehailia, D. Halliche, K. Bachari, Enhanced catalytic behaviour of surface dispersed nickel on LaCuO3 perovskite in the production of syngas: an expedient approach to carbon resistance during CO2 reforming of methane, Int. J. Hydrog. Energy 41 (2016) 2477–2486.
[24] G. Moradi, F. Khosravian, M. Rahmanzadeh, Effects of partial substitution of Ni by Cu in LaNiO3 perovskite catalyst for dry methane reforming, Chin. J. Catal. 33 (2012) 797–801.
[25] G.R. Moradi, M. Rahmanzadeh, F. Khosravian, The effects of partial substitution of Ni by Zn in LaNiO3 perovskite catalyst for methane dry reforming, J. CO2 Util. 6 (2014) 7–11.
[26] Z.G. Duma, X. Dyosiba, J. Moma, H.W. Langmi, B. Louis, K. Parkhomenko, N. M. Musyoka, Thermocatalytic hydrogenation of CO2 to methanol using Cu-ZnO bimetallic catalysts supported on Metal–Organic frameworks, Catalysts 12 (2022) 401.
[27] R. Pereñiguez, V.M. Gonzalez-delaCruz, A. Caballero, J.P. Holgado, LaNiO3 as a precursor of Ni/La2O3 for CO2 reforming of CH4: Effect of the presence of an amorphous NiO phase, Appl. Catal. B: Environ. 123-124 (2012) 324–332.
[28] J. Zhu, H. Li, L. Zhong, P. Xiao, X. Xu, X. Yang, Z. Zhao, J. Li, Perovskite oxides: preparation, characterizations, and applications in heterogeneous catalysis, ACS Catal. 4 (2014) 2917–2940.
[29] L. Jurado, V. Papaefthimiou, S. Thomas, A.-C. Roger, Upgrading syngas from wood gasification through steam reforming of tars over highly active Ni-perovskite catalysts at relatively low temperature, Appl. Catal. B: Environ. 299 (2021) 120687.
[30] A. Shahnazi, S. Firoozi, Improving the catalytic performance of LaNiO3 perovskite by manganese substitution via ultrasonic spray pyrolysis for dry reforming of methane, J. CO2 Util. 45 (2021) 101455.
[31] T. Maneerung, K. Hidajat, S. Kawi, LaNiO3 perovskite catalyst precursor for rapid decomposition of methane: Influence of temperature and presence of H2 in feed stream, Catal. Today 171 (2011) 24–35.
[32] R. Hu, R. Ding, J. Chen, J. Hu, Y. Zhang, Preparation and catalytic activities of the novel double perovskite-type oxide La2CuNiO6 for methane combustion, Catal. Commun. 21 (2012) 38–41.
[33] Z.G. Duma, J. Moma, H.W. Langmi, B. Louis, K. Parkhomenko, N.M. Musyoka, Towards high CO2 conversions using Cu/Zn catalysts supported on aluminum fumarate metal-organic framework for methanol synthesis, Catalysts 12 (2022) 1104.
[34] R. Guil-Lopez, J.A. Botas, J.L.G. Fierro, D.P. Serrano, Comparison of metal and carbon catalysts for hydrogen production by methane decomposition, Appl. Catal. A: Gen. 396 (2011) 40–51.
[35] A.M. Dunker, J.P. Ortmann, Kinetic modeling of hydrogen production by thermal decomposition of methane, Int. J. Hydrog. Energy 31 (2006) 1989–1998.
[36] S. Krzyżyński, M. Kozłowski, Activated carbons as catalysts for hydrogen production via methane decomposition, Int. J. Hydrog. Energy 33 (2008) 6172–6177.
[37] I. Suelves, J. Pinilla, M. Lázaro, R. Moliner, J. Palacios, Effects of reaction conditions on hydrogen production and carbon nanofiber properties generated by methane decomposition in a fixed bed reactor using a NiCuAl catalyst, J. Power Sources 192 (2009) 35–42.
[38] M.E. Rivas, C.E. Hori, J.L.G. Fierro, M.R. Goldwasser, A. Griboval-Constant, H2 production from CH4 decomposition: regeneration capability and performance of nickel and rhodium oxide catalysts, J. Power Sources 184 (2008) 265–275.
[39] L.S. Lobo, M.D. Franco, Kinetics of catalytic carbon formation on steel surfaces from light hydrocarbons, Catal. Today 7 (1990) 247–256.
[40] Q. Liu, P. Wu, J. He, C. Liu, W. Jiang, Catalytic decomposition of methane by two-step cascade catalytic process: simultaneous production of hydrogen and carbon nanotubes, Chem. Eng. Res. Des. 163 (2020) 96–106.
[41] P.E. Nolan, D.C. Lynch, A.H. Cutler, Carbon deposition and hydrocarbon formation on group viii metal catalysts, J. Phys. Chem. B 102 (1998) 4165–4175.
[42] E. Kukovitskii, L. Chernozatonskii, S. L'vov, N. Mel'Nik, Carbon nanotubes of polyethylene, Chem. Phys. Lett. 266 (1997) 323–328.
[43] N. Bayat, F. Meshkani, M. Rezaei, Thermocatalytic decomposition of methane to COx-free hydrogen and carbon over Ni–Fe–Cu/Al2O3 catalysts, Int. J. Hydrog. Energy 41 (2016) 13039–13049.
[44] D. Chen, K.O. Christensen, E. Ochoa-Fernández, Z. Yu, B. Tøtdal, N. Latorre, A. Monzón, A. Holmen, Synthesis of carbon nanofibers: effects of Ni crystal size during methane decomposition, J. Catal. 229 (2005) 82–96.
[45] Y. Yi, H. Liu, B. Chu, Z. Qin, L. Dong, H. He, C. Tang, M. Fan, L. Bin, Catalytic removal NO by CO over LaNi0.5M0.5O3 (M = Co, Mn, Cu) perovskite oxide catalysts: Tune surface chemical composition to improve N2 selectivity, Chem. Eng. J. 369 (2019) 511–521.
[46] C. Deng, J. Qian, C. Yu, Y. Yi, P. Zhang, W. Li, L. Dong, B. Li, M. Fan, Influences of doping and thermal stability on the catalytic performance of CuO/Ce 20 M 1 O x (M= Zr, Cr, Mn, Fe, Co, Sn) catalysts for NO reduction by CO, RSC Adv. 6 (2016) 113630–113647.
[47] I. Suelves, M.J. Lázaro, R. Moliner, B.M. Corbella, J.M. Palacios, Hydrogen production by thermo catalytic decomposition of methane on Ni-based catalysts: influence of operating conditions on catalyst deactivation and carbon characteristics, Int. J. Hydrog. Energy 30 (2005) 1555–1567.
[48] B. Gao, J. Deng, Y. Liu, Z. Zhao, X. Li, Y. Wang, H. Dai, Mesoporous LaFeO3 catalysts for the oxidation of toluene and carbon monoxide, Chin. J. Catal. 34 (2013) 2223–2229.
[49] A. Tarjomannejad, A. Niaei, A. Farzi, D. Salari, P.R. Zonouz, Catalytic oxidation of CO over LaMn 1− x B x O 3 (B= Cu, Fe) Perovskite-type oxides, Catal. Lett. 146 (2016) 1544–1551.
[50] S. Ahmed, A. Aitani, F. Rahman, A. Al-Dawood, F. Al-Muhaish, Decomposition of hydrocarbons to hydrogen and carbon, Appl. Catal. A: Gen. 359 (2009) 1–24.